

# Microscopic and Spectroscopic Analysis of the Solid Electrolyte Interphase at Hard Carbon Composite Anodes in 1 M NaPF<sub>6</sub>/Diglyme

Krishnaveni Palanisamy,<sup>[a]</sup> Sven Daboss,<sup>[a]</sup> Jan Romer,<sup>[a]</sup> David Schäfer,<sup>[b]</sup> Marcus Rohnke,<sup>[b]</sup> Jackson K. Flowers,<sup>[c]</sup> Stefan Fuchs,<sup>[c]</sup> Helge S. Stein<sup>+</sup><sup>[c, d]</sup> Maximilian Fichtner,<sup>[c, e]</sup> and Christine Kranz<sup>\*[a]</sup>

The formation of the solid electrolyte interphase (SEI) on HC composite electrodes plays a crucial role in enhancing the performance and operational stability of sodium (Na<sup>+</sup>) ion batteries. It has been demonstrated that for HC anodes improved electrochemical performance, e.g., increase in coulombic efficiency (CE) and improved rate performance have been achieved in ether-based electrolytes. Here, we investigate spray-coated HC composite electrodes charged at low and high current rates in 1 M sodium hexafluorophosphate (NaPF<sub>6</sub>) in diglyme using half-cell experiments. The pristine and cycled HC anodes were examined in terms of conductivity and their electrochemical properties after cycling. In 1 M NaPF<sub>6</sub> ether-

based electrolyte, the spray-coated HC composite electrodes (film thickness approx. 22.0 μm with an active mass loading of approx. 2.0 mg cm<sup>-2</sup>) reached a discharge capacity of 431 mA h g<sup>-1</sup> at 0.1 C that stays constant for 40 cycles, which is substantially higher than that obtained in carbonate-based electrolytes. We investigated the formed interphase using conductive atomic force microscopy (c-AFM), scanning electrochemical microscopy (SECM), X-ray photoelectron spectroscopy (XPS) and time-of-flight secondary-ion mass spectrometry (ToF-SIMS), revealing distinct differences for longer cycling and at varying current rates which indicates that the properties of the formed SEI layers are influenced by the formation conditions.

## Introduction

Sodium-ion batteries (SIBs) have gained among the post-lithium battery chemistries, significant interest not only due to concerns regarding potential supply risks for lithium, which may be in future even more a concern given the expanding field of applications for lithium-ion batteries (LIBs) in transportation and electricity sectors.<sup>[1]</sup> Recent progress in SIBs is demonstrated by a significant body of literature addressing half-cell and full-cell

studies but also by recent commercialization e.g., by companies and start-ups such as CATL (China), HiNa Battery Technology (China), Tiamat (France) and Faradion (UK) that are already producing cells. In terms of cost and resource analysis, SIBs offer interesting perspectives for the future.<sup>[2-4]</sup> While on the negative side, hard carbon (HC) composite electrodes<sup>[5]</sup> are predominantly used as other carbonaceous materials have insufficient storage capability for sodium, both polyanionic and layered electrode materials are used as cathodes.<sup>[6]</sup> We recently evaluated spray-coating as a method to produce thin film HC composite anodes with different compositions, controlled mass loading and thickness demonstrating high coulombic efficiency.<sup>[7]</sup> Spray-coating limits the mechanical stress, allows control of thickness and mass loading and gives access to the modification of substrates with various geometries by applying masks.

Similar to LIBs, the formation of a solid electrolyte interphase (SEI) plays a pivotal role in the overall performance of SIBs. A comprehensive understanding of the SEI formation on HC composite electrodes is still elusive, as the nature and composition of the SEI is dependent on many factors including the electrolyte formulation including its ionic conductivity, electronic resistance, stability and viscosity.<sup>[8]</sup> The SEI formation and composition in SIBs is more dynamic compared to LIBs, given a higher solubility of the SEI components<sup>[9,10]</sup> and differences in mechanical properties.<sup>[11]</sup> SEI formation is also strongly dependent on cell conditions and temperature.<sup>[12]</sup>

A critical challenge in developing new cell chemistries is the capacity loss during cycling, which is often related to maintaining a stable SEI layer without electrolyte depletion,<sup>[13]</sup> structural

[a] K. Palanisamy, Dr. S. Daboss, J. Romer, Prof. Dr. C. Kranz  
Institute of Analytical and Bioanalytical Chemistry, Ulm University, Albert-Einstein-Allee 11, 89081 Ulm, Germany  
E-mail: christine.kranz@uni-ulm.de

[b] D. Schäfer, Prof. Dr. M. Rohnke  
Institute of Physical Chemistry, Center for Materials Research, Justus-Liebig University of Giessen, Heinrich-Buff-Ring 17, 35392 Gießen, Germany

[c] J. K. Flowers, S. Fuchs, Prof. Dr. H. S. Stein,<sup>+</sup> Prof. Dr. M. Fichtner  
Helmholtz Institute Ulm, Helmholtz Str. 11, 89081 Ulm

[d] Prof. Dr. H. S. Stein<sup>+</sup>  
Department of Chemistry, Technical University of Munich, TUM, School of Natural Sciences, Lichtenbergstr. 4, 85748 Garching, Germany

[e] Prof. Dr. M. Fichtner  
Institute of Nanotechnology, Karlsruhe Institute of Technology, 76021 Karlsruhe, Germany

[+] present affiliation

 Supporting information for this article is available on the WWW under <https://doi.org/10.1002/batt.202300482>

 © 2024 The Authors. Batteries & Supercaps published by Wiley-VCH GmbH. This is an open access article under the terms of the Creative Commons Attribution Non-Commercial NoDerivs License, which permits use and distribution in any medium, provided the original work is properly cited, the use is non-commercial and no modifications or adaptations are made.

collapse of the active material<sup>[14]</sup> and electrode contact loss.<sup>[15]</sup> The effect of the used sodium salt such as sodium hexafluorophosphate ( $\text{NaPF}_6$ ), sodium bis(trifluoromethanesulfonyl)imide ( $\text{NaTFSI}$ ) and sodium perchlorate ( $\text{NaClO}_4$ ) on the SEI formation on HC was systematically investigated using different mixtures of alkyl carbonates, which revealed that the coulombic efficiency (CE) in the first cycles was strongly influenced by the nature of the anions.<sup>[16,17]</sup> The main components of the SEI were found to be double alkyl carbonates and linear carbonates exhibiting higher electrochemical reactivity (i.e., side reactions) towards HC. Also, the thermal stability for a given solvent was reported to be dependent e.g., on the used salt,<sup>[18]</sup> which is also in agreement with previous findings.<sup>[19]</sup>

In SIBs, the commonly used salts are  $\text{NaClO}_4$  and  $\text{NaPF}_6$  in a mixture of alkyl carbonate-based<sup>[20]</sup> or ether based solvents.<sup>[21,22]</sup> Glymes ( $\text{R}-[\text{OCH}_2\text{CH}_2]_n-\text{OR}$ ) as solvents have lately been studied for SIBs,<sup>[23–27]</sup> and recently also for Na–S batteries.<sup>[28]</sup> 1,2-Dimethoxyethane (monoglyme) and 1-methoxy-2-(2-methoxyethoxy)ethane (hereafter referred to as diglyme) are stable amphiphilic solvents,<sup>[29]</sup> with an electrochemical stability window of e.g., 0–4.4 V vs.  $\text{Na}^+/\text{Na}$  (with  $\text{NaPF}_6$ ).<sup>[21]</sup> Furthermore, glyme-based electrolytes are advantageous given their low viscosity, comparatively low vapor pressure, and good chemical and thermal stability.<sup>[29]</sup> SEI formation on HC has been controversially discussed in the literature for  $\text{NaPF}_6$  in diglyme.<sup>[21,30–32]</sup> While there are studies reporting a rapid capacity fading in half-cells with HC anodes, which was assumed is related to an unstable SEI,<sup>[21]</sup> other groups reported a beneficial thin SEI layer,<sup>[30]</sup> or no SEI layer on HC.<sup>[31]</sup> Recently, a study reported that diglyme is beneficial for forming a thin SEI with low internal resistance on HC anodes (vs.  $\text{Na}^+/\text{Na}$ ) in 1 M  $\text{NaPF}_6$  in diglyme when compared to 1 M  $\text{NaPF}_6$  in EC:DEC electrolyte.<sup>[32]</sup>

The characterization of the SEI on hard carbon anodes often involves techniques like electrochemical impedance spectroscopy (EIS)<sup>[33]</sup> providing information on charge transfer and SEI resistance, transmission electron microscopy (TEM)<sup>[34]</sup> for high-resolution imaging or X-ray photoelectron spectroscopy (XPS)<sup>[35]</sup> providing information of the chemical composition. Scanning probe microscopy such as atomic force microscopy (AFM) has

been used to map morphological changes, whereas electrochemical SPM techniques like scanning electrochemical microscopy (SECM) provide information on electron transfer in solution. For example, conductive (c)-AFM offers the benefit of visualizing electronic conductivity, providing information on the homogeneity and electronic insulating properties of the formed interphase. (c)-AFM has been employed at electrode materials used in LIBs to study for example the conductive/insulating properties of single-walled carbon nanotubes (SWCNTs) based anodes,<sup>[36]</sup>  $\text{Ni}_{0.1625}\text{Mn}_{0.675}\text{Co}_{0.1625}\text{CO}_3$  (NMC)<sup>[37]</sup> and  $\text{LiNi}_{1/3}\text{Mn}_{1/3}\text{Co}_{1/3}\text{O}_2$  (NMC) cathodes<sup>[38]</sup> after cycling. SECM<sup>[39]</sup> was so far mainly used for LIBs.<sup>[40–42]</sup> Only recently, our group investigated HC composite electrodes using combined AFM-SECM.<sup>[43]</sup>

Here, we present electrochemical studies as well as c-AFM and SECM measurements of pristine and cycled HC composite electrodes using a half-cell configuration in 1 M  $\text{NaPF}_6$  in diglyme at different cycling conditions and current rates (0.1 C to 5 C). Information on the storage and diffusion-controlled  $\text{Na}^+$  insertion processes were investigated via bulk electrochemical studies, whereas electronic conductivity and electron transfer kinetics derived from SECM provide insight into heterogeneity and properties of formed layers. The composition of the SEI was further analyzed by XPS and time-of-flight secondary-ion mass spectrometry (ToF-SIMS).

## Results and Discussion

### Electrochemical Results

Figure 1a shows the first three cycles of spray-coated HC composite electrodes cycled in 1 M  $\text{NaPF}_6$  in diglyme using a half-cell configuration. Similar half-cell studies have been reported in the literature,<sup>[21,32]</sup> and the observed behavior is in good agreement with previous studies. During the first cyclic voltammogram (CV) (black curve, started at 2.0 V vs.  $\text{Na}^+/\text{Na}$ ), a peak at 0.8 V vs.  $\text{Na}^+/\text{Na}$  indicates electrolyte decomposition. At lower potentials (0.25 V–0.01 V vs.  $\text{Na}^+/\text{Na}$ ),  $\text{Na}$  insertion and pore filling of  $\text{Na}$  ions into HC composite electrode occurs.<sup>[44]</sup> During the subsequent two cycles (overlapping red and blue

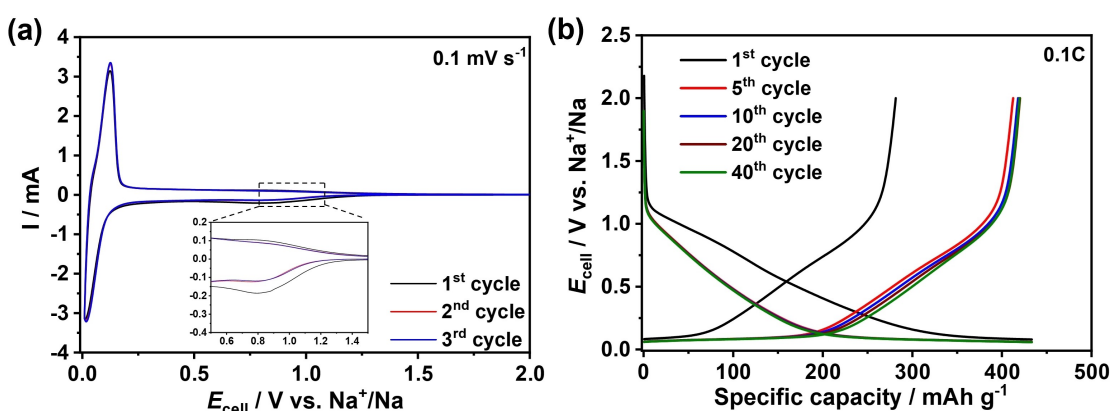


**Figure 1.** Electrochemical performance of spray-coated HC composite electrodes in 1 M  $\text{NaPF}_6$  in diglyme. a) Cyclic voltammograms (CVs), scan rate  $0.1 \text{ mV s}^{-1}$ , b) Galvanostatic discharge-charge curves at different cycles, current rate 0.1 C (current density,  $20 \text{ mA g}^{-1}$ ).

curves), the current response exhibits a decrease. The HC composite electrode might undergo reversible electrochemical reactions, which may lead to the formation of a thin<sup>[32]</sup> and stable SEI layer<sup>[21]</sup> during the first cycle.

The first discharge-charge curve of the HC at 0.1 C displays a difference in the voltage profile implying electrolyte decomposition or initial parasitic reactions consuming Na<sup>+</sup> ions as depicted in Figure 1b. During the first cycle, an initial coulombic efficiency (CE) of approximately 65% is observed. Subsequent cycling led to an increase in CE to 95% (5<sup>th</sup> cycle), 96% (10<sup>th</sup> cycle), 97% (20<sup>th</sup> cycle) and 97% (40<sup>th</sup> cycle), respectively, which we attribute to the stabilization of the SEI layer during cycling. Interestingly, a capacity retention of almost 99% was observed after 40 cycles.

We further examined capacity changes under different current rates to investigate the differences in electrochemical Na<sup>+</sup> storage in 1 M NaPF<sub>6</sub> in diglyme. The 1<sup>st</sup>, 5<sup>th</sup> and 10<sup>th</sup> cycles of 0.1 C and 5 C current rate cycled samples are shown in Figure S1. The first cycle displays a different voltage profile when compared to the 5<sup>th</sup> and 10<sup>th</sup> cycle, which we associate with the formation of a SEI layer in the first discharge cycle (Figure S1). During the initial discharge cycle at 5 C current rate, an increase in capacity of 509 mAhg<sup>-1</sup> was observed. This capacity increase is attributed to the rapid transfer of Na<sup>+</sup> ions at this high current rate, which was also previously observed by Yin et al.<sup>[32]</sup> However, the following cycles (5<sup>th</sup> and 10<sup>th</sup> cycle) show a clear decrease in capacity to around 430 mAhg<sup>-1</sup>. The observed capacity drop at the high current rate may be related to the fact that the electrolyte decomposition occurs more

rapidly than the solvents can reach the electrode surface.<sup>[45,46]</sup> Similar capacity values were observed for 0.1 C rate without decreasing capacity values from 1<sup>st</sup> to 5<sup>th</sup> and 10<sup>th</sup> cycles (Figure 1b). Overall, the HC samples cycled at high current rate in 1 M NaPF<sub>6</sub> in diglyme electrolyte reveal that there is a complex reciprocation between current rates, SEI layer formation, Na<sup>+</sup> ion transfer, and electrolyte decomposition in SIBs.

The insertion of Na<sup>+</sup> ions into HC composite electrodes was investigated via CV using different scan rates (0.05, 0.1, 0.2, 0.4, 0.6, 0.8 and 1 mV s<sup>-1</sup>) in 1 M NaPF<sub>6</sub> in diglyme, as shown in Figure 2. From the scan-rate dependent CVs, the ratio of diffusion- and surface-controlled processes can be obtained as previously shown for HC anode electrodes.<sup>[32]</sup> The charge storage capacity obtained from the CVs can be divided into two parts: diffusion-controlled capacity and surface-controlled capacity (capacitance). The ratio between the two processes can be obtained by analyzing the relationship between the current (I) and the scan rate (v) from the CVs recorded at different scan rates using the following Equation (1).<sup>[47,48]</sup>

$$I(v) = a v^b \quad (1)$$

A b-value of 0.5 reflects diffusion-controlled behavior, whereas a value of 1.0 implies a capacitance-controlled mechanism. Figure 2b displays a plot of log (i<sub>cathodic</sub>) vs log (v) with b=0.63, illustrating that the HC composite electrodes exhibit surface and diffusion-controlled processes, as previously reported for HC derived from phenolic resin.<sup>[32]</sup>

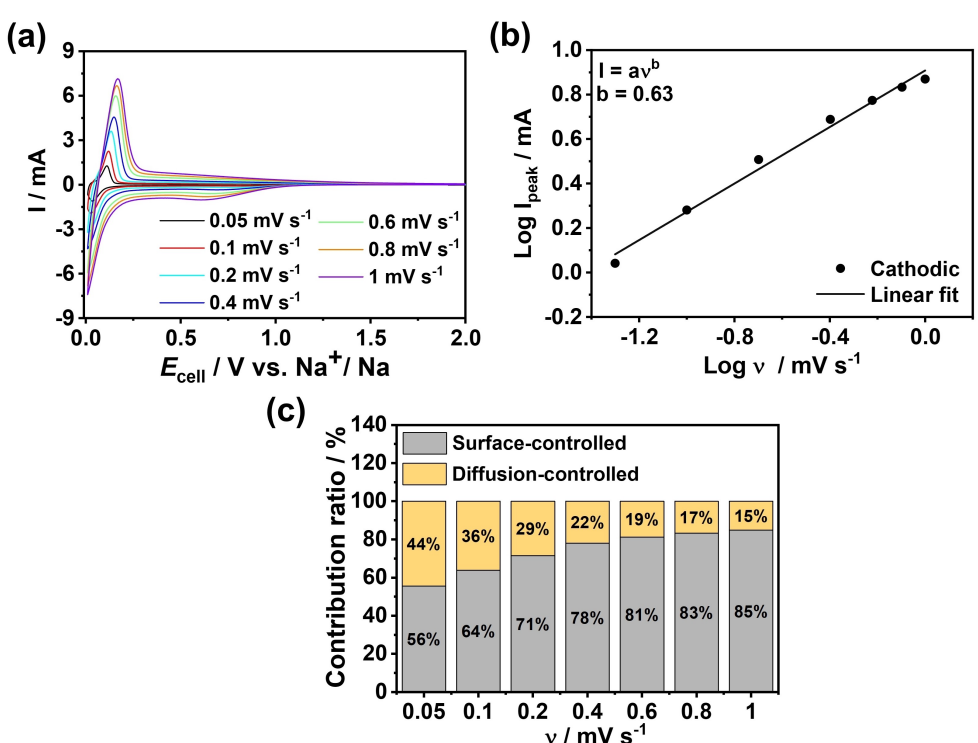


**Figure 2.** (a) Cyclic voltammograms with sweep rates of 0.05, 0.1, 0.2, 0.4, 0.6, 0.8 and 1 mV s<sup>-1</sup>. (b) b-Values (slopes) obtained from logarithmic plots of the peak current (i<sub>cathodic</sub>) vs. the scan rate, coefficient of determination R<sup>2</sup>=0.99, (c) Normalized capacity contribution ratio of capacitive and diffusion storage of the HC electrode at different scan rates in 1 M NaPF<sub>6</sub> in diglyme.

The current response at different scan rates (0.05, 0.1, 0.2, 0.4, 0.6, 0.8 and 1 mVs<sup>-1</sup>) was used to obtain the capacitive contribution to the current response, as shown in Equations (2) and (3).<sup>[49,50]</sup>

$$I(v) = k_1 v + k_2 v^{1/2} \quad (2)$$

$$\frac{I(v)}{v^{1/2}} = k_1 v^{1/2} + k_2 \quad (3)$$

Where  $v$ ,  $I(v)$ ,  $v^{1/2}$ ,  $v$ ,  $k_1$ , and  $k_2$  are the scan rate, current at a given potential, and coefficients reflecting the contribution fraction from the surface-controlled and bulk (diffusion)-controlled processes. The linear fitting of the  $I(v)/v^{1/2}$  and  $v^{1/2}$  yields the  $k_1$  value. The grey marked area in the bar diagram shown in Figure 2c are the contributions of  $k_1 v$  (surface-controlled charge storage) for scan rates of 0.05, 0.1, 0.2, 0.4, 0.6, 0.8, and 1 mVs<sup>-1</sup>, which reflect 56, 64, 71, 78, 81, 83 and 85% of the overall capacitance for the HC composite electrode, respectively. With increasing scan rate to 0.4, 0.6, 0.8 and 1 mVs<sup>-1</sup>, the surface-controlled charge storage became more dominant, which is in agreement with previous studies for HC vs. Na<sup>+</sup>/Na in 1 M NaPF<sub>6</sub> in diglyme.<sup>[32]</sup> This behavior may account for the higher specific capacity observed for the 1<sup>st</sup> cycle at high current rate (5 C) visible in Figure S1b.

The surface morphologies of individual HC particles of the cycled composite electrodes were analyzed using AFM in non-contact mode in dependence of cycling numbers and current rates, as shown in Figure S2. The mean surface roughness ( $S_a$ ) of single particles after 1, 5, 10, 20, and 40 cycles show no significant changes (Figure S3). Similarly, for the  $S_a$  values of the HC electrodes cycled at various current rates (0.5 C, 1 C, 2 C, 3 C, 4 C, and 5 C), no significant change was observed, (Figure S4). To minimize artifacts, only small areas with one or few HC

particles have been investigated to obtain possible surface roughness changes of HC particles.

### c-AFM

In the following, c-AFM images of the pristine and cycled HC composite electrodes were recorded to map changes in the electronic conductivity of the HC anodes, which indicates the formation of an electronically blocking interphase after the 1<sup>st</sup> cycle. Despite the challenges of possible artifacts when investigating real battery electrodes with high surface roughness,<sup>[36]</sup> c-AFM maps e.g., of single HC particles provide nanoscale spatial information on electronic conductivity. Hence, to minimize artifacts, again only small areas with one or few HC particles have been investigated. Figure S5 shows a secondary electron image (scanning electron microscopy, SEM) of the pristine HC composite electrode which allows to estimate the size of the differently oriented particles (purple: CMC/CC, grey: HC). Figure S6 shows larger topography and conductivity image (scan area, 20×20  $\mu\text{m}^2$ ) of a pristine HC composite electrode. c-AFM analysis was conducted of small areas with single or few HC particles. Figure 3 depicts the topography and conductivity images of pristine HC composite electrode and after cycling at different cycling periods. The observed changes in conductivity of the pristine sample may be associated to changes in the contact area between the conductive tip and sample given the morphology and orientation of the HC particle in the composite material or binder moieties at the HC particles. To mitigate this source of artifacts, the composite electrodes could be embedded and polished,<sup>[51]</sup> however thus may alter the behavior and is challenging for larger electrodes used here in the half-cell studies. We recently demonstrated for an embedded and polished sample cycled in NaClO<sub>4</sub>/propylene carbonate that

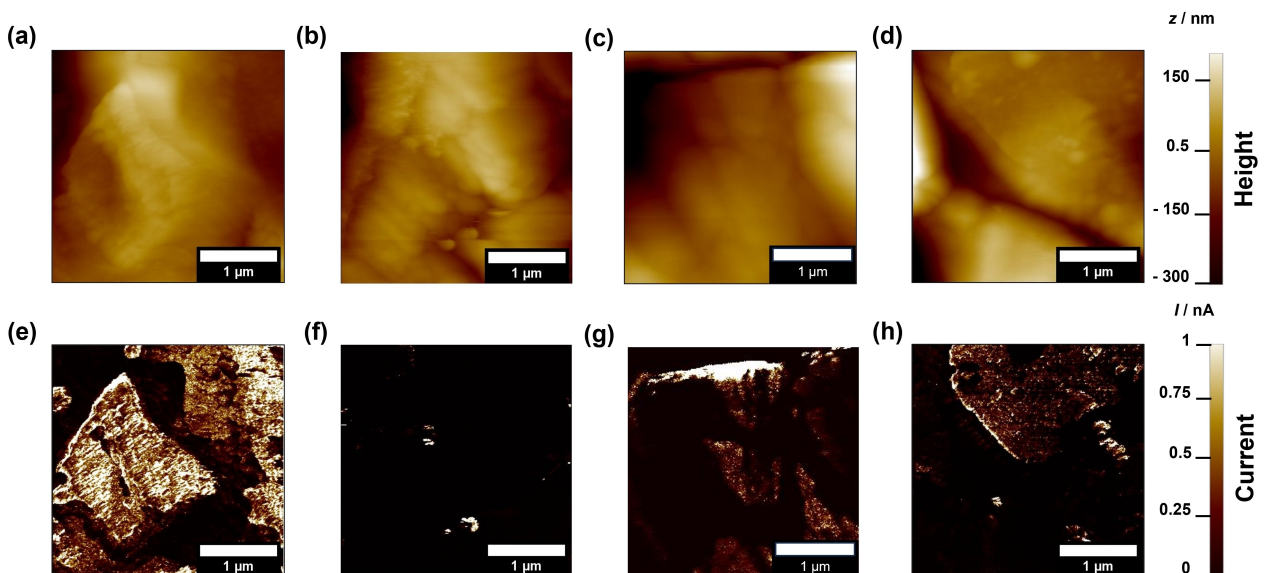


**Figure 3.** C-AFM images of HC composite electrodes before and after cycling in 1 M NaPF<sub>6</sub> in diglyme, topography of (a) Pristine, (b) 1 cycle, (c) 10 cycles and (d) 40 cycles. Corresponding conductivity image of (e) pristine, (f) 1 cycle, (g) 10 cycles and (h) 40 cycles. Applied potential: 0.5 V.

conductivity domains observed for cycled samples are attributed to the formation of an insulating SEI on the HC particles.<sup>[43]</sup> Despite possible artifacts on the non-embedded samples, we observed a significant change in electronic conductivity after the composite electrodes were cycled, particularly after the first cycle. The electronic conductivity dropped by  $96 \pm 2\%$  (from  $1.01 \pm 0.16$  nA to  $0.04 \pm 0.02$  nA (eight different spots were evaluated per sample) after the first cycle, which indicates that a uniform electronically blocking layer was formed. The observed small areas of high conductivity (Figure 3f) may be associated to artifacts of the small features with significant height change. Interestingly, in the following cycles, mixed conductivity of the HC particles was observed. After 10 cycles, it appears that the HC particles are only partly blocked and the observed high conductivity at the edge of the particle (upper part in Figure 3g) is probably related to artifacts, whereas after 40 charge-discharge cycles, clearly mixed conductive and non-conductive areas are visible, which may be attributed to the formation of an inhomogeneous SEI layer. Individual conducting HC particles show a reduced conductivity compared to the pristine one ( $0.27 \pm 0.08$  nA,  $73 \pm 11\%$  decrease), which may be associated with partial dissolution of the formed SEI at longer cycling. This is in line with the literature, where challenges of forming a stable SEI at HC anodes is discussed given the higher solubility of inorganic SEI components in SIBs compared to LIBs.<sup>[52]</sup> SEI constituents e.g., inorganic (non-conductive) compounds, like  $\text{Na}_2\text{CO}_3$  or  $\text{NaF}$  were also observed in the XPS spectra (Figure 6). These compounds were reported in the literature using diglyme electrolyte in a system comprising a bulk Bi cathode.<sup>[27]</sup> As shown in Figure S7b, the HC anode cycled at a current rate of 5 C exhibits an inhomogeneous insulating layer after 10 cycles, comparable with the electrode shown in Figure 3h (40 cycles at 0.1 C). The current decreased for the anode cycled at 5 C to  $0.48 \pm 0.16$  nA, ( $55 \pm 17\%$  decrease compared to the pristine electrode). We also conducted a Pearson correlation analysis to interpret dissimilarities in the AFM images to ensure the absence of artifacts.<sup>[36]</sup> The contribution of abnormal current signals to the current map is low indicated by a narrow and straight line (Figure S8).

### Scanning Electrochemical Microscopy (SECM)

Although SIBs are amongst the most developed post-Li ion batteries, so far there are only a quite limited number of SECM studies on SIBs reported in the literature<sup>[43,53]</sup> when compared to LIBs.<sup>[41,54–61]</sup> In contrast to c-AFM, SECM is a non-contact SPM technique and the measurements provide information on local heterogeneities of electron transfer kinetics at the electrode surface, which may not be accessible with bulk electrochemical measurements. The local electron transfer kinetics at pristine and cycled HC composite electrodes (0.1 C) was investigated via SECM in feedback mode using ferrocene as redox active species. For a pristine HC composite electrode (Figure 4a), the, at the tip oxidized redox active species, can be re-reduced at the conductive electrode surface, when the tip is positioned close to the sample surface. This results in a local increase in

concentration of the redox mediator within the small gap between the SECM tip and sample surface, which leads to an increased faradaic current at the SECM microelectrode (positive SECM feedback effect). The normalized current responses indicate a homogeneous reactivity of the mapped surface area ( $I_T/I_{T\infty} > 1$ , where  $I_T/I_{T\infty}$  reflects the ratio of the current at the specific distance and diffusion-limited current at quasi-infinite distance to the sample). The observed variations in the current may to some extent be related to the surface morphology as the image was recorded in constant height mode, scanning the microelectrode (radius,  $r_T = 1.5 \mu\text{m}$ ) in a fixed tilt-corrected plane across the sample surface. Given the surface roughness and the size of the SECM microelectrode, there may be some convolution of topographical effects with the observed current.  $S_a$  values of single particles are in the range of hundred nm (Figure S3–S4), however for larger areas ( $100 \mu\text{m} \times 100 \mu\text{m}$ ) as investigated via SECM,  $S_a$  values of  $3.04 \pm 0.98 \mu\text{m}$  ( $n=3$ ) have to be considered. To avoid the potential effect of surface roughness, also current-distance curves<sup>[62]</sup> (approach curves, where the normalized distance  $L = d/r_T$  is the ratio of distance  $d$  and  $r_T$ ) were recorded at different spots of the HC composite electrodes (Figure 4e–h). The theoretical approach curves are displayed at red solid curves. Locations where approach curves were recorded are marked as '+' (black) in the SECM image of the pristine sample (Figure 4a). Figure 4e shows an exemplary experimental approach curve (black dotted line) with the corresponding standard deviation (shaded grey areas of the 8 curves recorded at the different spots).

The obtained positive feedback response at different positions of the HC composite electrode is attributed to the conductive nature of the HC particles and conductive carbon. Given the size of the UME and the fact of overlapping diffusion profiles at randomly aligned HC particles, individual particles are not resolved. In contrast to the pristine electrode, the recorded faradaic current is significantly decreased in the SECM image of the composite electrode recorded after one cycle (Figure 4b). We attribute this decrease in faradaic current to the decomposition of the electrolyte forming an insulating SEI layer at the anode surface,<sup>[55]</sup> which is in line with the c-AFM data shown in Figure 3b and f. The blocking nature of the formed layer is also evident in the approach curves, again recorded at 8 different locations (marked with '+'), which all exhibit hindered electron transfer (Figure 4f, shaded gray area shows again the corresponding standard deviation). Interestingly, for the HC composite electrode, which was cycled 10 times, an increase in electron transfer was obtained across the imaged sample area, as depicted in Figure 4c. This increase may be attributed to the partial dissolution of the SEI layer, which is also evident in the corresponding approach curves, as illustrated in Figure 4g (again, the grey shaded area reflects the standard deviation taking all recorded curves into account). Similar phenomena have been documented in recent studies at Si–C anodes for LIBs,<sup>[55]</sup> which revealed the heterogeneity of the SEI layer formation on the Si–C anode after a few cycles. After 40 cycles, the SECM image reveals mixed responses. The recorded approach curves showed both positive (marked as black '+',  $n=5$ ) and negative feedback currents (marked as red '+',  $n=4$ )

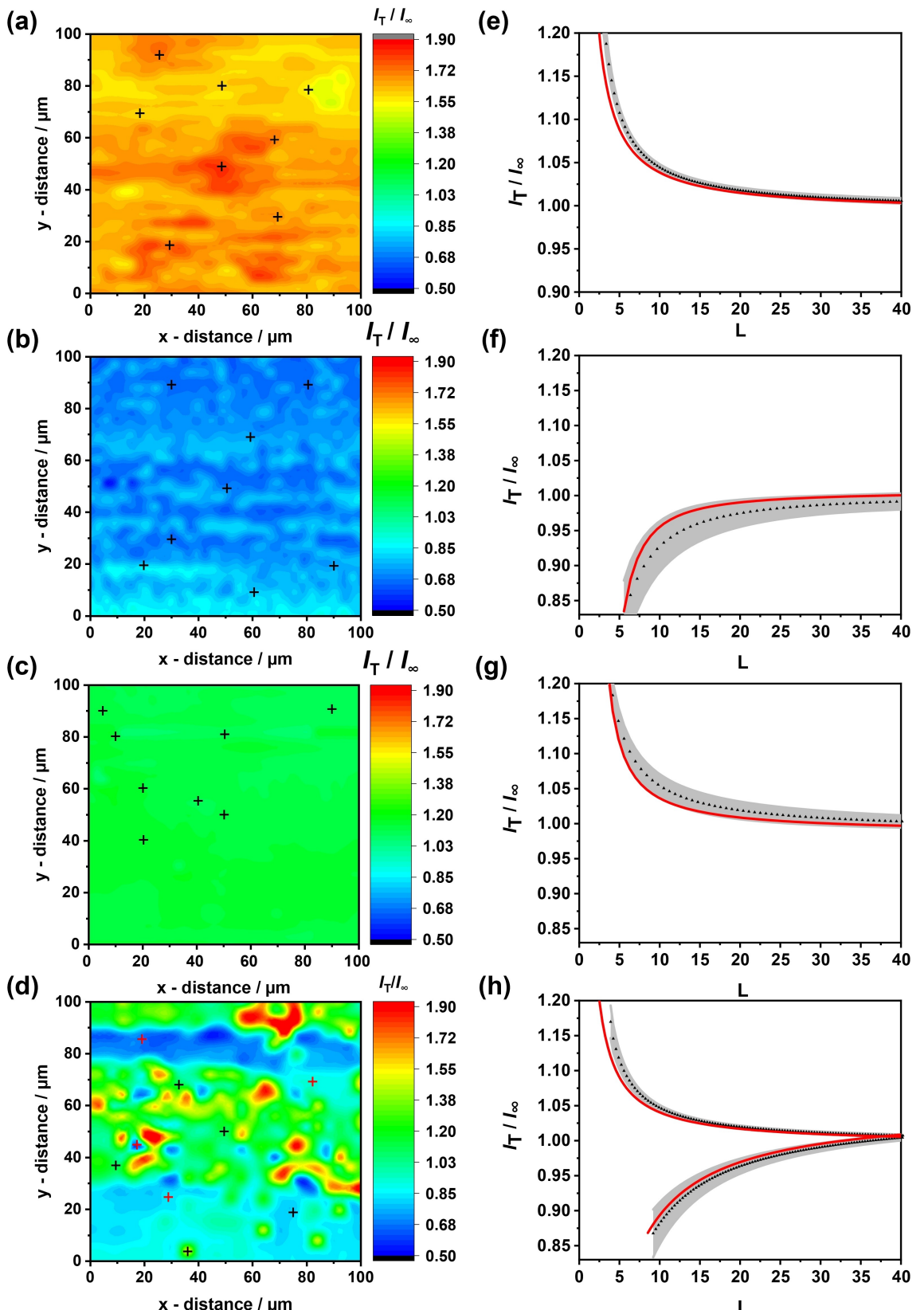


**Figure 4.** SECM feedback mode images and approach curves recorded at marked areas: (a) SECM image of a pristine HC composite electrode. Marked points indicate locations where approach curves were recorded. (e) Experimental approach curves at pristine HC composite electrode (black) and corresponding theoretical fit (red), standard deviation is shown as shaded grey area ( $n=8$ ). (b-d) SECM image of cycled HC composite electrode (0.1 C): (b) 1 cycle, (c) 10 cycles and (d) 40 cycles in 1 M NaPF<sub>6</sub> in diglyme, marked points indicate the locations where approach curves were recorded with negative feedback (red) and with positive feedback (black). (f-h) Experimental approach curves revealing negative and positive feedback (black) with corresponding fits (red) of the cycled HC composite electrode. The standard deviation is shown as shaded grey area.

at different spots of the HC composite electrode (Figure 4h, grey shaded areas reflect the standard deviations). It appears that a heterogenous SEI layer was formed after 40 cycles, which is in excellent agreement with our c-AFM data (Figure 3h). These measurements were repeated with two other sets of newly prepared spray-coated HC composite electrodes (using two different sets of slurries). As shown in Figure S9 and S10, the same trend was observed. The samples which were objected to 1 cycle showed significantly hindered electron transfer, whereas after 10 cycles, it appears that the SEI layer is dissolved as positive feedback is observed. The samples, which were cycled 40 times show mixed behavior, again pointing towards a heterogeneous SEI layer.

From SECM approach curves, quantitative data on the effective heterogeneous rate constant of electron transfer can be derived, which has been shown for e.g., graphite anodes for LIBs.<sup>[58,63]</sup> The quantitative kinetic values are obtained by fitting experimental approach curves to corresponding theoretical expressions.<sup>[64]</sup> The dimensionless heterogeneous rate constant parameter  $\kappa$  can be derived from Equation 4.<sup>[65]</sup>

$$I_T(L, RG, \kappa) \approx I_T^0 \left( L + \frac{1}{\kappa}, RG \right) + \frac{I_T^{ins}(L, RG) - 1}{(1 + 2.47 RG^{0.31} L \kappa)(1 + L^{0.006 RG + 0.113} \kappa^{-0.0236 RG + 0.91})} \quad (4)$$

The  $\kappa$  values for the pristine electrode are significantly higher compared to the obtained values after 1 cycle (pristine:  $\kappa = 1.75 \pm 0.11$  ( $n=8$ ), 1 cycle:  $\kappa = 0.37 \pm 0.22$  ( $n=8$ )). After 10 cycles, the HC composite electrode reveals an increase of  $\kappa = 1.29 \pm 0.19$  ( $n=8$ ), which may indicate the dissolution of the SEI formed during the first cycles, leaving a thin SEI layer, which still allows electron transfer to reduce the redox mediator at the electrode surface. The measurements were repeated at different areas showing the same trend (data not shown). After 40 cycles, mixed electron transfer kinetics at the cycled HC composite electrode is observed with  $\kappa = 1.12 \pm 0.04$  ( $n=5$ ) for the positive approach curves and  $\kappa = 0.38 \pm 0.18$  ( $n=4$ ) for the negative approach curves.

The corresponding effective heterogeneous kinetics constant  $k_{eff}$  ( $k_{eff} = \kappa \frac{D}{r}$ ) was extracted using a diffusion coefficient for ferrocene of  $D = 2.24 \cdot 10^{-5} \text{ cm}^2 \text{s}^{-1}$ <sup>[66]</sup> and SECM tip radius,  $r_T = 1.5 \mu\text{m}$ . The  $k_{eff}$  value of the cycled HC composite electrode applying 1 cycle is  $0.0559 \pm 0.0328 \text{ cm}^2 \text{s}^{-1}$  compared to the pristine electrode with  $k_{eff} = 0.2612 \pm 0.0161 \text{ cm}^2 \text{s}^{-1}$ . After 10 cycles, the HC composite electrode shows an increase in  $k_{eff}$  of  $0.1927 \pm 0.0283 \text{ cm}^2 \text{s}^{-1}$ , when compared to 1 cycle, possibly due to the dissolution of the inorganic SEI components (see also XPS data displayed in Figure 6b). The  $k_{eff}$  values for the HC composite electrode after 40 cycles are  $0.1680 \pm 0.0066 \text{ cm}^2 \text{s}^{-1}$  for the positive feedback approach curves and  $0.0571 \pm 0.0271 \text{ cm}^2 \text{s}^{-1}$  for negative feedback approach curves. Hence, it seems that the SEI undergoes changes over longer cycling, resulting in more heterogeneous layers characterized by both insulating and conducting areas, which is again in agreement with the performed c-AFM measurements. Approach curves were recorded at two additionally cycled HC composite electro-

des (see Figure S9 and 10, spots are marked with crosses). The derived  $k_{eff}$  values are summarized in Figure 5 and the  $\kappa$  and  $k_{eff}$  in Table S1.

### XPS Analysis

We also investigated the chemical composition of the pristine and cycled HC composite electrodes by XPS and the obtained fits of the spectra for the detected elements are shown in Figure 6. The survey spectrum of all samples is shown in Figure S11. The assigned peaks are presented in Table S2. The C1s spectrum of the pristine electrode is consistent with data from the literature for CMC mixed with CC<sup>[67]</sup> with the addition of a  $\text{CF}_3$  peak at 293.5 eV. Fluorocarbon contamination of the pristine electrode is discussed in detail in the Supporting Information (see Figure S12). The sample displays a small  $\text{Na}^{1s}$  peak at 172 eV, which is attributed to the sodiated CMC. After one cycle, the  $\text{sp}^2$  hard carbon peak is significantly smaller and shifts from 284.4 eV to 283.4 eV, indicating the formation of an SEI layer and sodiation of the hard carbon.<sup>[19,68,69]</sup> The F1s spectrum consists of three peaks, including components at 687.9 eV and 684.4 eV, in addition to the smaller C–F peak at 288.9 eV. The peak at 684.4 eV is assigned to  $\text{NaF}$  formation, while the peak at 687.9 eV is commonly associated with  $\text{PF}_6^-$  anion or partial decompositions of the salt. Stoichiometric analysis of the relative peak intensities suggests that about one third of the sodium signal of the sample can be ascribed to  $\text{NaF}$ , while the identity of the remainder depends on the nature of the phosphorous-containing  $\text{NaPF}_6$  decomposition products. A pair of P2p peaks appear, at 137.6 eV and 132.9 eV respectively. The peak at 137.6 eV is generally ascribed to  $\text{NaPF}_6$ , though this is not distinguishable from  $\text{PF}_5$  or other similar decomposition products, and is commonly labelled as  $\text{Na}_x\text{PF}_y$ .<sup>[17]</sup> The peak at 132.9 eV is characteristic for phosphate, the identity of which is not precisely defined in the literature.

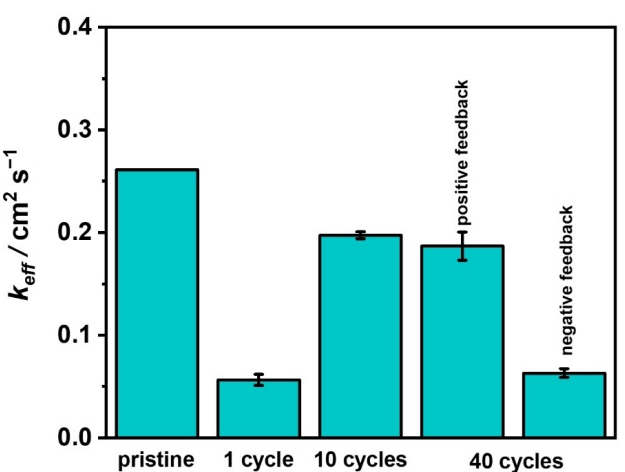
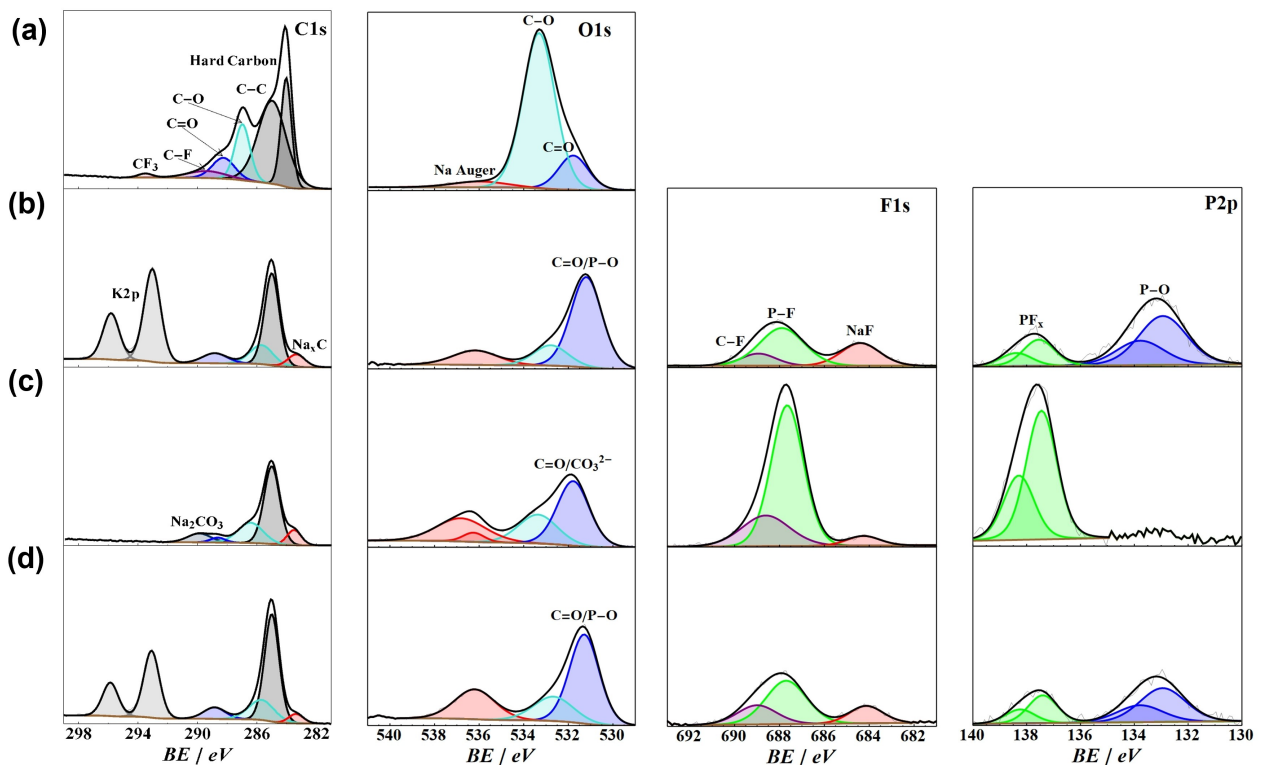


Figure 5. Bar diagram of the effective heterogeneous kinetics constant  $k_{eff}$  values for pristine and cycled HC composite electrodes. Error bars reflect values retrieved from the recorded approach curves of three different samples cycled 1, 10 or 40 times.



**Figure 6.** XPS spectra of the pristine and cycled HC composite electrodes in 1 M  $\text{NaPF}_6$  in diglyme. (a) Pristine, (b) 1 cycle, (c) 40 cycles and (d) 5 C (10 cycles).

Luo et al.<sup>[70]</sup> and He et al.<sup>[71]</sup> ascribe the 137 eV peak to  $\text{Na}_x\text{PF}_y\text{O}_z$ , also giving the possible decomposition path. Pan et al.,<sup>[68]</sup> and Eshetu et al.<sup>[17]</sup> report XPS data with the  $\text{Na}_x\text{PF}_y\text{O}_z$  peak occurring at a higher binding energy and ascribe the peak around 133 eV to simple phosphate.

After 40 cycles, the F1s NaF peak is significantly decreased, and a C1s carbonate peak at 289.9 eV is visible, suggesting that  $\text{Na}_2\text{CO}_3$  has replaced NaF and phosphate as the primary surface sodium component of the SEI.<sup>[19,67]</sup> The hard carbon peak at 283.5 eV is of slightly higher magnitude than the sample after 1 cycle, indicating again that the formed SEI layer is heterogeneous for longer cycling. Additionally, an anomalously large quantity of  $\text{Na}_x\text{PF}_y$  is observed (the F:P ratio of roughly 3:1), whereas the phosphate peak is entirely absent after 40 cycles.

The XPS spectra of the sample cycled at 5 C (10 cycles) do not reveal any features directly attributable to the increased cycling rate. The spectra are very similar to those of the sample after 1 cycle, though with a notably smaller hard carbon peak (C1s), which indicates an increased thickness of the SEI layer. The smaller NaF and phosphate peaks and larger Cl2p and Na1s peaks may be attributed to further NaCl formation from possible KCl contamination (see Supporting Information).

### ToF-SIMS

Pristine samples and samples cycled with different parameters (0.1 C for 1 and 40 cycles and 5 C for 10 cycles) were also analyzed by static time-of-flight secondary ion mass spectrometry (ToF-SIMS). Hereby, the sample surface is probed with a very low dose of so-called primary ions that cause a collision cascade at the sample surface. Some of the particles that leave the surface because of the impact are ions, which are collected by an electrical field, separated in a mass analyzer according to their mass to charge ratio and finally detected. More background information to the application of this method in battery research was recently published by Lombardo et al.<sup>[72]</sup>

The obtained mass spectra are depicted in Figure 7. In Figure 7a, the spectrum of the pristine sample is shown consisting only of peaks that can be assigned to hydrocarbons, and oxygenated hydrocarbons originating from the partly adsorptive covered hard carbon particles as well as from the oxygen containing binder. The negligibly small  $\text{F}^-$  signal in the ToF-SIMS spectrum of the pristine sample points towards that the observed contamination in the XPS data originate from the transfer process to the XPS instrument, which is different for the composite electrodes and the individual components. In contrast to XPS, where the detection limit is in the sub percent range, ToF-SIMS is very sensitive (ppm range) for fluorine. Most

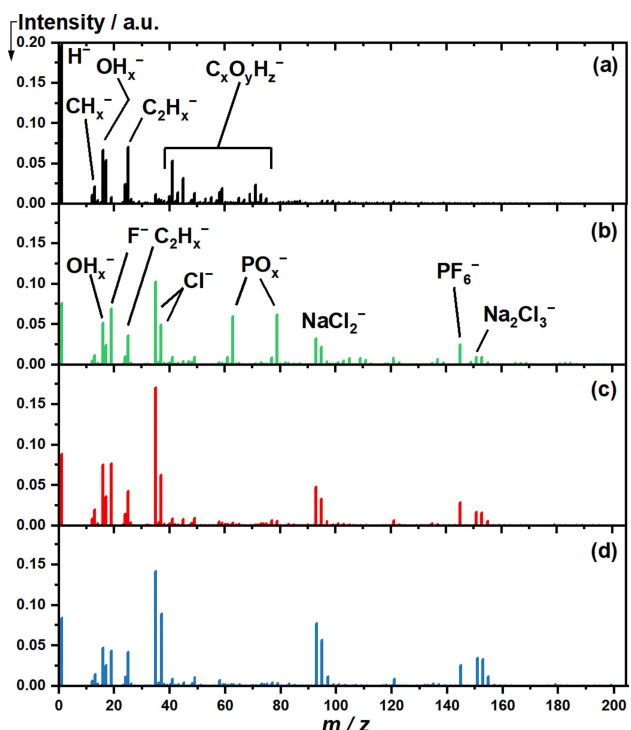


**Figure 7.** Comparative ToF-SIMS surface spectra in negative secondary ion mode of (a) pristine, b) 1 cycle, c) 40 cycles, and d) 10 cycles (5 C). The spectra are being displayed as line spectra with respect to the average peak areas of 5 measurements per electrode normalized to the total ion intensity.

mass fragments extracted from the surface of cycled hard carbon samples in negative ion mode can be attributed to the chemical compounds NaCl and NaF. As stated in the Supporting Information, contaminations like chlorine (Cl) may have been introduced by the counter electrode (Na) containing potassium (K) (up to 500 ppm) and Cl (up to 100 ppm) according to the manufacturer's data sheet. These components must be produced during cycling on the electrode surface and accumulated on the SEI surface. The overall differences in the ToF-SIMS spectra of differently cycled samples, Figure 7(b-d), are rather small. Comparing the relative intensities of fragments corresponding to the low- $m/z$  hydrocarbons  $\text{CH}_x^-$  and  $\text{C}_2\text{H}_x^-$ , similar values are observed in the spectra while the intensities of heavier hydrocarbon fragments drop significantly with the cycle number.

The remaining of the former can be attributed to unavoidable surface adsorption from the glove box atmosphere. The heavier hydrocarbon fragments originate obviously from the formed SEI layer, which slightly changes its composition during the cycling process. Since information on SEI thickness is not easily accessible, it cannot be ruled out that in the case of an SEI only a few monolayers thick, these signals come from the hard carbon underneath. However, the minor changes of signal intensities of the inorganic components as well as the XPS data indicate a thicker (several nm) and covering SEI layer. The conservation of the relative intensities for all cycled samples is observable for the fragments  $\text{Cl}^-$  and  $\text{NaCl}_2^-$ . The fragments can be assigned to reaction products of the conductive salt, the

chlorine impurities, and the electrolyte. The main difference between all spectra is related to the variation of the relative intensity of the fragments  $\text{F}^-$  and  $\text{Na}_3\text{F}_4^-$ , respectively. . However, this may be accredited to statistical irregularities. It is assumed in the literature that the lateral SEI composition is inhomogeneous.<sup>[68]</sup>

Measurements in positive ion mode reveal  $\text{Na}_2\text{O}$ ,  $\text{NaOH}$  and  $\text{Na}_2\text{CO}_3$  as major chemical components at the sample surface as depicted in Figure S13. Here, the relative intensities for the shown fragments increase with an increasing number of cycles but also for the sample cycled at 5 C. This leads to the assumption that the SEI composition changes slightly during cycling and  $\text{Na}_2\text{CO}_3$  is continuously being formed. The change of the SEI composition is in line with the obtained SECM data.

## Conclusions

We investigated the performance of spray-coated HC composite anodes in 1 M  $\text{NaPF}_6$  in diglyme, using bulk electrochemical, microscopic, spectroscopic and spectrometric methods. Cycling at different current rates had no substantial influence on the surface roughness of the HC particles of the cycled HC composite electrodes, as shown by AFM results. The  $S_a$  values indicate good stability of the electrodes under the studied conditions. The c-AFM and SECM measurements give insight into local heterogeneity of the formed SEI in dependence of the cycling number. Although c-AFM is conducted in air and is a contact SPM technique, the data of both studies reveal quite similar results, indicating a homogenous coverage of individual HC particles after 1 cycle and partial dissolution after further cycling. However, it should be noted that the XPS data indicate a steadily increasing SEI layer thickness up to 40 cycles, as judged by the sodiated HC peak. The changes in the reversible charging and discharging processes at higher current rate (5 C) and longer cycles (40 cycles) are related to the formation of  $\text{Na}_2\text{CO}_3$  and NaF components, which could be identified by chemical analysis using XPS and ToF-SIMS. To our best knowledge, there is no SPM study on the stability of the SEI cycled in 1 M  $\text{NaPF}_6$  in diglyme at HC composite electrodes cycled in half-cell configuration, yet. Hence, our studies shine some light on the dynamics of the SEI formation during the first 40 cycles.

## Experimental Section

### Materials

HC active material was obtained from Kuraray (Kuranode 5  $\mu\text{m}$  (type II), Japan), acetonitrile, diglyme, sodium carboxymethyl cellulose (CMC) and tetrabutylammonium hexafluorophosphate (TBAPF<sub>6</sub>) were obtained from Sigma Aldrich, Germany. Sodium and ferrocene (Fc) were purchased from Alfa Aesar, Germany. Carbon black conductive carbon (CC) was purchased from Cabot Corporation (Vulcan XC72R, USA).

## Electrode and Electrolyte Preparation

HC composite electrodes were prepared by spray-coating.<sup>[7]</sup> In short, Na-based CMC was dissolved in water, CC and HC mixed in the corresponding ratio (85 % active material, 5 % binder, 10% CC) and added to the solution. After stirring the solution for 48 h at 50 °C, isopropyl alcohol (70%, ≥98%) was added and the mixture was filled into the spray-gun. 3 passes were applied, and the spray-coated electrodes were dried overnight at RT and then vacuum dried at 80 °C for 12 h leading to a film thickness of 22.0±0.5 µm ( $n=3$ ) of the composite electrode. The electrolyte for galvanostatic cycling was prepared using 1 M NaPF<sub>6</sub> in anhydrous diglyme. The redox mediator solution for the SECM experiments was prepared using 0.01 M Fc/0.1 M TBAPF<sub>6</sub> in acetonitrile.

## Electrochemical Tests

HC composite anodes with a mass loading of 2.0±0.1 mg cm<sup>-2</sup> ( $n=3$ ) were used and mounted in a Swagelok cell assembled in an Ar-filled glove box (MBraun, O<sub>2</sub> <0.1 ppm, H<sub>2</sub>O <0.01 ppm) in a two-electrode configuration using a Na-metal cathode and a glass-fiber separator (Whatman, GF/F). Electrochemical tests were performed on a battery testing station using a BCS-805 Biologic battery test system (Biologic BS-805, Biologic, France) at room temperature (25 °C) in galvanostatic mode between 0.01–2.0 V vs. Na<sup>+</sup>/Na at 20 mA g<sup>-1</sup>. Cyclic voltammetry (CV) was performed in the potential range of 0.01–2.0 V vs. Na<sup>+</sup>/Na at a scan rate of 0.05, 0.1, 0.2, 0.4, 0.6, 0.8, and 1 mV s<sup>-1</sup>. For characterization steps after cycling, the electrodes were carefully rinsed with dimethyl carbonate (DMC) which was shown to not alter the surface composition<sup>[20]</sup> and dried at 80 °C for 20 minutes.

## Atomic Force Microscopy

The HC composite electrodes before and after cycling were analyzed using an AFM (Park NX10, Park Systems, South Korea) located in an Ar-filled glove box (MBraun, O<sub>2</sub> <0.1 ppm, H<sub>2</sub>O <0.1 ppm). AFM probes (NCL, Nanosensors, Switzerland) with a resonant frequency of 190 kHz, a nominal tip radius of 10 nm and a nominal spring constant of 48 N m<sup>-1</sup> were used in non-contact mode at a scan speed of 0.4 Hz to determine the surface roughness values. The force constant of each cantilever was determined prior to the measurement using the thermal noise method.<sup>[73]</sup> Roughness parameters before and after cycling were calculated from 5 × 5 µm<sup>2</sup> areas (five different spots of one sample (512×512 pixel)). c-AFM was performed using conductive diamond coated cantilevers (Bruker AD-2.8-AS-3U, France) with a resonant frequency of 65 kHz, a nominal tip radius of 10 nm and a spring constant of 2.8 N m<sup>-1</sup> with an applied bias of 0.5 V in contact mode. The measured area for the surface conductivity measurements was 20×20 µm<sup>2</sup> for the HC composite electrodes. 0.5 µm<sup>2</sup> areas were selected and the current values on individual particles for the small areas were averaged. AFM images were analyzed using Parks imaging processing tool for SPM data (XEI 5.2, Park Systems, South Korea) and MountainsSPM (version 9.1.9908, Digital Surf, France).

## Scanning Electrochemical Microscopy

Approach curves and SECM maps of pristine and cycled HC composite electrodes were recorded in feedback mode in 0.01 M Fc in MeCN/0.1 M TBAPF<sub>6</sub>. A Pt UME ( $r=1.5\text{ }\mu\text{m}$ ) served as a working electrode, an Ag/AgCl as a reference electrode and a Pt wire as counter electrode. All measurements were performed with the Sensolytics SECM software (version 2.2.3.3 Sensolytics, Germany) with an applied potential of 0.5 V vs. Ag/AgCl. Maps of

100×100 µm<sup>2</sup> were recorded with an increment of 3 µm and a scanning speed of 2 µm s<sup>-1</sup>. Different random assigned locations were chosen to perform approach curves with an approach speed of 2 µm s<sup>-1</sup>. Approach curves were analyzed using the model of Amphlett and Denault either for insulator or conductors<sup>[65]</sup> using MiRa (Version 2.0, G. Wittstock, University of Oldenburg, Germany).

## XPS Measurements

XPS measurements were performed for cycled HC composite electrodes with a near ambient pressure (NAP)-XPS (Specs EnviroESCA, Germany). The NAP-XPS is part of the platform for accelerated electrochemical energy storage Research (PLACES/R) at Helmholtz Institute Ulm.<sup>[74]</sup> Spectra of another pristine electrode and of the individual compounds (HC, CC, CMC and NaPF<sub>6</sub> powder samples) were taken with a commercial UHV system (SPECS) with a base pressure of 2×10<sup>-10</sup> mbar using a monochromatized X-ray source (SPECS XR50 M, Al-K $\alpha$  and Ag-K $\alpha$ , FOCUS 500 X-ray monochromator) and a hemispherical analyzer (SPECS, DLSEGD-Phoibos-Has3500). Fine spectra ( $n=10$ ) were taken to capture the C1s, O1s, F1s, Na1s, P2p, Cl2p and K2p lines. CasaXPS (version 2.3.23, Japan) software was used to fit the data for all fits.

## Secondary Ion Mass Spectrometry

Electrodes for ToF-SIMS analysis were handled under argon atmosphere in a glove box and transported in a transfer shuttle (VCT 500, Leica Microsystems, Germany) under inert gas conditions to the SIMS machine. Static ToF-SIMS measurements were performed in positive and negative ion mode using a ToF-SIMS M6 machine (IONTOF, Germany), which is equipped with a 30 keV Bi nanoprobe as analysis gun. A pulsed Bi<sub>3</sub><sup>+</sup> primary ion beam scanned a surface area of 100×100 µm<sup>2</sup> with 128×128 pixels at a cycle time of 100 µs until a dose density of 1.00×10<sup>13</sup> ions/cm<sup>2</sup> was reached. Charge compensation was carried out with a low energetic electron flood gun. The achieved mass resolution was better than  $m/\Delta m = 6,000$  (FWHM) at  $m/z$  92.92 (NaCl<sub>2</sub><sup>-</sup>) in negative ion mode and better than  $m/\Delta m = 5,000$  (FWHM) at  $m/z$  80.96 (Na<sub>2</sub>Cl<sup>+</sup>) in positive ion mode. For data analysis SurfaceLab (version 7.2, IONTOF GmbH, Germany) was used by which the surface spectra were calibrated to the mass signals of the fragments CH<sup>-</sup>, C<sub>2</sub>H<sub>3</sub><sup>-</sup>, CH<sub>3</sub>O<sup>-</sup>, C<sub>2</sub>H<sub>3</sub>O<sup>-</sup>, C<sub>4</sub>H<sub>3</sub>O<sup>-</sup> and C<sub>6</sub>H<sub>5</sub><sup>-</sup> for the spectra in negative ion mode. For the spectra in positive ion mode the same fragments with the respective polarity were used: CH<sup>+</sup>, C<sub>2</sub>H<sub>3</sub><sup>+</sup>, CH<sub>3</sub>O<sup>+</sup>, C<sub>2</sub>H<sub>3</sub>O<sup>+</sup>, C<sub>4</sub>H<sub>3</sub>O<sup>+</sup> and C<sub>6</sub>H<sub>5</sub><sup>+</sup>.

## Acknowledgements

The Focused Ion Beam Center UUlm is acknowledged. This work contributes to the research performed at CELEST (Center for Electrochemical Energy Storage Ulm - Karlsruhe) and was funded by the Deutsche Forschungsgemeinschaft (DFG, German Research Foundation) under Germany's Excellence Strategy – EXC 2154 – Project number 390874152 (POLIS Cluster of Excellence). MR thanks the DFG for funding the Hybrid SIMS under grant no. INST 162/544-1 FUGG. Open Access funding enabled and organized by Projekt DEAL.

## Conflict of Interests

The authors declare that they have no known competing financial interests or personal relationships that could have appeared to influence the work reported in this paper.

## Data Availability Statement

The data that support the findings of this study are openly available in Zenodo at Zenodo DOI: 10.5281/zenodo.8348207, reference number 351.

**Keywords:** Hard carbon composites · diglyme · SEI layer · conductive AFM · SECM

- [1] M. Wahid, D. Puthusseri, Y. Gawli, N. Sharma, S. Ogale, *ChemSusChem* **2018**, *11*, 506–526.
- [2] E. J. Berg, C. Villevieille, D. Streich, S. Trabesinger, P. Novák, *J. Electrochem. Soc.* **2015**, *162*, A2468–A2475.
- [3] C. Vaalma, D. Buchholz, M. Weil, S. Passerini, *Nat. Rev. Mater.* **2018**, *3*, 18013.
- [4] J. Peters, D. Buchholz, S. Passerini, M. Weil, *Energy Environ. Sci.* **2016**, *9*, 1744–1751.
- [5] E. Irisarri, A. Ponrouch, M. R. Palacin, *J. Electrochem. Soc.* **2015**, *162*, A2476–A2482.
- [6] R. Dugas, B. Zhang, P. Rozier, J. M. Tarascon, *J. Electrochem. Soc.* **2016**, *163*, A867–A874.
- [7] K. Palanisamy, S. Daboss, D. Schäfer, M. Rohnke, L. Derr, M. Lang, R. Schuster, C. Kranz, *Batteries & Supercaps* **2024**, *7*, e202300402.
- [8] A. Ponrouch, E. Marchante, M. County, J.-M. Tarascon, M. R. Palacín, *Energy Environ. Sci.* **2012**, *5*, 8572.
- [9] R. Mogensen, D. Brandell, R. Younesi, *ACS Energy Lett.* **2016**, *1*, 1173–1178.
- [10] D. I. Iermakova, R. Dugas, M. R. Palacín, A. Ponrouch, *J. Electrochem. Soc.* **2015**, *162*, A7060–A7066.
- [11] L. Schafzahl, H. Ehmann, M. Kriegbaum, J. Sattelkow, T. Ganner, H. Plank, M. Wilkening, S. A. Freunberger, *Chem. Mater.* **2018**, *30*, 3338–3345.
- [12] S. K. Heiskanen, J. Kim, B. L. Lucht, *Joule* **2019**, *3*, 2322–2333.
- [13] R. Mogensen, J. Maibach, A. J. Naylor, R. Younesi, *Dalton Trans.* **2018**, *47*, 10752–10758.
- [14] Z. Yu, J. Song, D. Wang, D. Wang, *Nano Energy* **2017**, *40*, 550–558.
- [15] Z. Liu, T. Lu, T. Song, X.-Y. Yu, X. W. (David) Lou, U. Paik, *Energy Environ. Sci.* **2017**, *10*, 1576–1580.
- [16] G. G. Eshetu, S. Grugeon, H. Kim, S. Jeong, L. Wu, G. Gachot, S. Laruelle, M. Armand, S. Passerini, *ChemSusChem* **2016**, *9*, 462–471.
- [17] G. G. Eshetu, T. Diemant, M. Hekmatfar, S. Grugeon, R. J. Behm, S. Laruelle, M. Armand, S. Passerini, *Nano Energy* **2019**, *55*, 327–340.
- [18] A. Ponrouch, D. Monti, A. Boschin, B. Steen, P. Johansson, M. R. Palacín, *J. Mater. Chem. A* **2015**, *3*, 22–42.
- [19] A. Ponrouch, R. Dedryvère, D. Monti, A. E. Demet, J. M. Ateba Mba, L. Croguennec, C. Masquelier, P. Johansson, M. R. Palacín, *Energy Environ. Sci.* **2013**, *6*, 2361–2369.
- [20] J. Fondard, E. Irisarri, C. Courrèges, M. R. Palacin, A. Ponrouch, R. Dedryvère, *J. Electrochem. Soc.* **2020**, *167*, 070526.
- [21] K. Westman, R. Dugas, P. Jankowski, W. Wieczorek, G. Gachot, M. Morcrette, E. Irisarri, A. Ponrouch, M. R. Palacín, J. M. Tarascon, P. Johansson, *ACS Appl. Energ. Mater.* **2018**, *1*, 2671–2680.
- [22] G. G. Eshetu, G. A. Elia, M. Armand, M. Forsyth, S. Komaba, T. Rojo, S. Passerini, *Adv. Energy Mater.* **2020**, *10*, 2000093.
- [23] B. Jache, J. O. Binder, T. Abe, P. Adelhelm, *Phys. Chem. Chem. Phys.* **2016**, *18*, 14299–14316.
- [24] I. Hasa, X. Dou, D. Buchholz, Y. Shao-Horn, J. Hassoun, S. Passerini, B. Scrosati, *J. Power Sources* **2016**, *310*, 26–31.
- [25] Z. W. Seh, J. Sun, Y. Sun, Y. Cui, *ACS Cent. Sci.* **2015**, *1*, 449–455.
- [26] Y. E. Zhu, L. Yang, X. Zhou, F. Li, J. Wei, Z. Zhou, *J. Mater. Chem. A* **2017**, *5*, 9528–9532.
- [27] C. Wang, L. Wang, F. Li, F. Cheng, J. Chen, *Adv. Mater.* **2017**, *29*, 1–7.
- [28] L. Carbone, S. Munoz, M. Gobet, M. Devany, S. Greenbaum, J. Hassoun, *Electrochim. Acta* **2017**, *231*, 223–229.
- [29] S. Tang, H. Zhao, *RSC Adv.* **2014**, *4*, 11251–11287.
- [30] H. Alptekin, H. Au, E. Olsson, J. Cottom, A. C. Jensen, T. F. Headen, Q. Cai, A. J. Drew, M. Crespo Ribadeneyra, M. Titirici, *Adv. Mater. Interfaces* **2022**, *9*, 2101267.
- [31] J. Pan, Y. Sun, Y. Yan, L. Feng, Y. Zhang, A. Lin, F. Huang, J. Yang, *JACS Au* **2021**, *1*, 1208–1216.
- [32] X. Yin, Z. Wang, Y. Liu, Z. Lu, H. Long, T. Liu, J. Zhang, Y. Zhao, *Nano Res.* **2023**, *16*, 10922–10930.
- [33] P. Lu, C. Li, E. W. Schneider, S. J. Harris, *J. Phys. Chem. C* **2014**, *118*, 896–903.
- [34] M. Carboni, J. Manzi, A. R. Armstrong, J. Billaud, S. Brutt, R. Younesi, *ChemElectroChem* **2019**, *6*, 1745–1753.
- [35] H. S. Hirsh, B. Sayahpour, A. Shen, W. Li, B. Lu, E. Zhao, M. Zhang, Y. S. Meng, *Energy Storage Mater.* **2021**, *42*, 78–87.
- [36] G. Park, Y. Choi, S. Shin, Y. Lee, S. Hong, *ACS Appl. Mater. Interfaces* **2022**, *14*, 30639–30648.
- [37] S. Y. Luchkin, M. A. Kirsanova, D. A. Aksyonov, S. A. Lipovskikh, V. A. Nikitina, A. M. Abakumov, K. J. Stevenson, *ACS Appl. Energ. Mater.* **2022**, *5*, 7758–7769.
- [38] A. Sakuda, M. Otoyama, T. Yamaoka, H. Ito, Y. Inagi, M. Tatsumisago, A. Hayashi, *J. Phys. Chem. C* **2021**, *125*, 2841–2849.
- [39] A. J. Bard, F. R. F. Fan, J. Kwak, O. Lev, *Anal. Chem.* **1989**, *61*, 132–138.
- [40] G. Zampardi, S. Klink, V. Kuznetsov, T. Erichsen, A. Maljusch, F. La Mantia, W. Schuhmann, E. Ventosa, *ChemElectroChem* **2015**, *2*, 1607–1611.
- [41] H. Bültner, F. Peters, J. Schwenzel, G. Wittstock, *Angew. Chem. Int. Ed.* **2014**, *53*, 10531–10535.
- [42] K. Mahankali, N. K. Thangavel, L. M. Reddy Arava, *Nano Lett.* **2019**, *19*, 5229–5236.
- [43] S. Daboss, T. Philipp, K. Palanisamy, J. Flowers, H. S. Stein, C. Kranz, *Electrochim. Acta* **2023**, *453*, 142345.
- [44] Y. Kim, K. H. Ha, S. M. Oh, K. T. Lee, *Chem. A Eur. J.* **2014**, *20*, 11980–11992.
- [45] S. M. Oh, J. Song, S. Lee, I. C. Jang, *Electrochim. Acta* **2021**, *397*, 139269.
- [46] W. Huang, P. M. Attia, H. Wang, S. E. Renfrew, N. Jin, S. Das, Z. Zhang, D. T. Boyle, Y. Li, M. Z. Bazant, B. D. McCloskey, W. C. Chueh, Y. Cui, *Nano Lett.* **2019**, *19*, 5140–5148.
- [47] H. Lindström, S. Södergren, A. Solbrand, H. Rensmo, J. Hjelm, A. Hagfeldt, S. E. Lindquist, *J. Phys. Chem. B* **1997**, *101*, 7710–7716.
- [48] C. N. Gannett, L. Melecio-Zambrano, M. J. Theibault, B. M. Peterson, B. P. Fors, H. D. Abruna, *Mater. Reports Energy* **2021**, *1*, 100008.
- [49] V. Augustyn, P. Simon, B. Dunn, *Energy Environ. Sci.* **2014**, *7*, 1597–1614.
- [50] P. Yu, C. Li, X. Guo, *J. Phys. Chem. C* **2014**, *118*, 10616–10624.
- [51] S. Y. Luchkin, S. A. Lipovskikh, N. S. Katorova, A. A. Savina, A. M. Abakumov, K. J. Stevenson, *Sci. Rep.* **2020**, *10*, 1–10.
- [52] L. A. Ma, A. J. Naylor, L. Nyholm, R. Younesi, *Angew. Chem. Int. Ed.* **2021**, *60*, 4855–4863.
- [53] D. Sarbapalli, Y.-H. Lin, S. Stafford, J. Son, A. Mishra, J. Hui, A. Nijamudheen, A. I. B. Romo, Z. T. Gossage, A. M. van der Zande, J. L. Mendoza-Cortes, J. Rodríguez-López, *J. Electrochem. Soc.* **2022**, *169*, 106522.
- [54] E. Ventosa, E. Madej, G. Zampardi, B. Mei, P. Weide, H. Antoni, F. La Mantia, M. Muhler, W. Schuhmann, *ACS Appl. Mater. Interfaces* **2017**, *9*, 3123–3130.
- [55] N. Jiyane, E. García-Quismondo, E. Ventosa, W. Schuhmann, C. S. Santos, *Batteries & Supercaps* **2023**, *6*, e202300126.
- [56] E. dos Santos Sardinha, M. Sternad, H. M. R. Wilkening, G. Wittstock, *ACS Appl. Energ. Mater.* **2019**, *2*, 1388–1392.
- [57] E. García-Quismondo, S. Alvarez-Conde, G. Garcia, J. I. Medina-Santos, J. Palma, E. Ventosa, *ACS Appl. Mater. Interfaces* **2022**, *14*, 43319–43327.
- [58] C. S. Santos, A. Botz, A. S. Bandarenka, E. Ventosa, W. Schuhmann, *Angew. Chem. Int. Ed.* **2022**, *61*, e202202744.
- [59] B. Krueger, K. K. Rücker, G. Wittstock, *ACS Appl. Energ. Mater.* **2022**, *5*, 3724–3733.
- [60] H. Bültner, F. Peters, G. Wittstock, *Energy Technol.* **2016**, *4*, 1486–1494.
- [61] T. Tarnev, P. Wilde, A. Dopilka, W. Schuhmann, C. K. Chan, E. Ventosa, *ChemElectroChem* **2020**, *7*, 665–671.
- [62] G. Wittstock, M. Burchardt, S. E. Pust, Y. Shen, C. Zhao, *Angew. Chem. Int. Ed.* **2007**, *46*, 1584–1617.
- [63] X. Zeng, D. Liu, S. Wang, S. Liu, X. Cai, L. Zhang, R. Zhao, B. Li, F. Kang, *ACS Appl. Mater. Interfaces* **2020**, *12*, 37047–37053.
- [64] J. L. Amphlett, G. Denuault, *J. Phys. Chem. B* **1998**, *102*, 9946–9951.
- [65] R. Cornut, C. Lefrou, *J. Electroanal. Chem.* **2008**, *621*, 178–184.

- [66] Y. Wang, E. I. Rogers, R. G. Compton, *J. Electroanal. Chem.* **2010**, *648*, 15–19.
- [67] A. Darwiche, L. Bodenes, L. Madec, L. Monconduit, H. Martinez, *Electrochim. Acta* **2016**, *207*, 284–292.
- [68] Y. Pan, Y. Zhang, B. S. Parimalam, C. C. Nguyen, G. Wang, B. L. Lucht, *J. Electroanal. Chem.* **2017**, *799*, 181–186.
- [69] M. Carboni, J. Manzi, A. R. Armstrong, J. Billaud, S. Brutti, R. Younesi, *ChemElectroChem* **2019**, *6*, 1745–1753.
- [70] J. Luo, Y. Zhang, E. Matios, P. Wang, C. Wang, Y. Xu, X. Hu, H. Wang, B. Li, W. Li, *Nano Lett.* **2022**, *22*, 1382–1390.
- [71] J. He, T. Tao, F. Yang, Z. Sun, *ChemSusChem* **2022**, *15*, e202102522.
- [72] T. Lombardo, F. Walther, C. Kern, Y. Moryson, T. Weintraut, A. Henss, M. Rohnke, *J. Vac. Sci. Technol. A* **2023**, *41*, 053207.
- [73] J. L. Hutter, J. Bechhoefer, *Rev. Sci. Instrum.* **1993**, *64*, 1868–1873.
- [74] H. S. Stein, A. Sanin, F. Rahamanian, B. Zhang, M. Vogler, J. K. Flowers, L. Fischer, S. Fuchs, N. Choudhary, L. Schroeder, *Curr. Opin. Electrochem.* **2022**, *35*, 101053.

Manuscript received: October 17, 2023

Revised manuscript received: December 22, 2023

Accepted manuscript online: January 2, 2024

Version of record online: February 13, 2024